Atomic structure and microstructures of supertetragonal multiferroic $BiFeO_3$ thin films

F. Pailloux,[1,2,*] M. Couillard,[2,3] S. Fusil,[4] F. Bruno,[4] W. Saidi,[1] V. Garcia,[4] C. Carrétéro,[4] E. Jacquet,[4] M. Bibes,[4] A. Barthélémy,[4] G. A. Botton,[2] and J. Pacaud[1]

[1]*Institut Pprime, UPR3346 CNRS-Université de Poitiers, Material Physics and Mechanics Department, Bd M. & P. Curie, 86962 Futuroscope-Chasseneuil, France*

[2]*Canadian Center for Electron Microscopy, Brockhouse Institute for Materials Research, McMaster University, 1280 Main Street West, Hamilton, Ontario L8S4M1, Canada*

[3]*National Research Council Canada, 1200 Montreal Road, Ottawa, ON, K1A 0R6, Canada*

[4]*Unité Mixte de Physique CNRS/Thales, Campus de l'Ecole Polytechnique, 1 Avenue Fresnel, 91767 Palaiseau, France and Université Paris-Sud, 91405, Orsay, France*

(Received 25 June 2013; revised manuscript received 17 February 2014; published 12 March 2014)

We revisit the atomic structure and microstructure of the so-called supertetragonal phases of highly strained epitaxial $BiFeO_3$ thin films. Quantitative atomic resolution scanning transmission electron microscopy is used to directly image the atomic positions. A crystallographic phase suggested by electron diffraction and predicted by *ab initio* calculations is evidenced. Microtwins are reported in thickest films. Electron energy loss spectroscopy is further employed to reveal subtle electronic structure features, which, interpreted in a framework of antiferrodistortive distortions coupling with the substrate, point towards a phase closer to the $P4mm$ purely tetragonal phase.

DOI: 10.1103/PhysRevB.89.104106 PACS number(s): 77.55.Nv, 68.37.Ma, 68.55.Nq, 77.80.bn

I. INTRODUCTION

Functional materials based on complex oxides have been attracting considerable attention over the last decades because of their outstanding physical properties such as high-temperature superconductivity, colossal magnetoresistance, piezoelectricity, and multiferroic behavior. Because of its high transition temperatures (ferroelectric up to T_C close to 1100 K and antiferromagnetic up to T_N close to 645 K), bismuth ferrite has emerged as a promising magnetoelectric material in spintronics [1]. Its electromechanical properties have also imposed $BiFeO_3$ (BFO) as a lead-free alternative for piezoelectric applications [2].

Whereas bulk BFO crystallizes in the rhombohedral $R3c$ space group with a G-type antiferromagnetic order and a cycloid modulation in the $\langle 111\rangle$-pseudo-cubic direction [3], other phases can be stabilized by strain engineering. Depending on the misfit between the substrate and the BFO: a so-called R-like phase (derived from the $R3c$ bulk structure) is favored for misfit up to about 4% (typical for $SrTiO_3$ substrate); above this value (for instance, $LaAlO_3$ [LAO] substrate used in this paper), T-like phases (derived from the $P4mm$ tetragonal phase theoretically predicted [4]) corresponding to a jump in the c/a ratio from 1.06 to 1.2 can be stabilized [5,6]. Accordingly, several authors have experimentally observed the occurrence of both distorted phases [2,7–12]. The films grown near this 4% threshold exhibit a mixture of both phases under the form of a morphotropic phase boundary (MPB) driven by strain [2]. This configuration (mixture of phases) has been invoked to explain huge piezoelectric response due to its similarity with composition-driven MPBs observed in $PbMgNbO_3$-$PbTiO_3$ or $PbZnNbO_3$-$PbTiO_3$. A piezomagnetic coupling of these phases has also been suspected to enhance the magnetization of the samples [13,14]. Very recently, the influence of the octahedra rotation coupling at the film $BiFeO_3$//$SrTiO_3$ interface has been reported [15] in line with the antiferrodistortive coupling previously observed [16] and theoretically predicted [17].

The stability of T-like phases has been analyzed by density functional theory (DFT) calculations [5,6] giving a rather flat energy landscape for the different calculated structures, which makes most of them relevant candidates for films grown under high compressive strain. This multiplicity of possible phases has been proposed to explain the discrepancy between experimentally measured and theoretically predicted polarizations [5]. It has also been an issue in the accurate determination of the space group in which the T phases crystallize (Cc or Cm), irrespective of the type of characterization technique, whether structural [with transmission electron microscopy (TEM), x-ray, or neutron diffraction] or through magnetic measurements because of subtle structural differences and the similar predicted polar moments of about 150 $\mu C/cm^2$ of these two specific phases. Nevertheless, both theoretical calculations and experimental observations point toward a huge tetragonal distortion of the pseudocubic unit cell with a c/a ratio greater than 1.24 for biaxially strained BFO films on LAO [5,11]; this distortion being associated with a shift of the Fe atom [12]. It has recently been reported that the oxygen octahedra surrounding the Fe experience also a huge distortion (a large shift of the apical oxygen) that leads to a FeO_5 pyramidal unit rather than the octahedral FeO_6 unit commonly depicted in cubic perovskites [10,12]. The main difference between the Cc and Cm phases considered here and derived from *ab initio* calculations [5] lies in the antiferrodistortive rotation of the O pyramids due to the M_3^+ in-phase mode in one direction in Cm and the R_4^+ out-of-phase in two directions in Cc. The absence of all O-pyramid tilting would lead to the $P4mm$ tetragonal phase already evoked. Accompanying these oxygen ions displacements, iron-ion shift also occurs in the plane of the film giving rise to different in-plane polarizations M_A and M_C, respectively, for the monoclinic Cc and Cm phases. The

*frederic.pailloux@univ-poitiers.fr

sensitivity of this in-plane component of the polarization has been studied as a function of the epitaxial strain sustained by the film [18,19]. It is worth pointing out that some doubts remain concerning the phases in which the supertetragonal phase of BFO crystallize when subjected to a high epitaxial stress (when epitaxially grown on LAO substrate, for instance): whereas some studies [6,7] have proposed the possible coexistence of the *Cm* and *Cc* phases, more recent studies [12,18] tend to promote the *Cc* space group calculated in Ref. [20]. Very recently, the structure of BFO//LAO interfaces has been investigated by spherical aberration (Cs)-corrected annular bright field-scanning transmission electron microscopy (ABF-STEM) [21] and by a combination of high-angle annular dark field (HAADF)-STEM and electron energy loss spectroscopy (EELS) experiments [22]. A cation interdiffusion has been evidenced in Ref. [22], and a continuous expansion of the BFO lattice associated with FeO_6 distortions and correlated to a polarization relaxation has been reported in Ref. [21].

In this paper, we focus on the supertetragonal (T-like) phase of BFO grown on LAO and provide direct evidences of the space group in which this T phase does crystallize, by combining energy filtered electron diffraction (EFED) and HAADF/ABF STEM. We also highlight structural fluctuations that occur in thicker films whereby the resulting microstructure is more complex than the one commonly depicted. The comparison between theoretically predicted and experimentally measured polarizations is usually based on the assumption of defect free samples; our observations on thick films suggest that structural defects could contribute to explaining the reported discrepancies. Finally, the structural analysis of thin films reveals departures from the phase observed in the thicker films: high-resolution (HR)-EELS evidences subtle electronic structure deviations close to the film/substrate interface of thinnest films. The implications of our findings on the polarization of BFO films are discussed.

II. EXPERIMENTAL DETAILS

A. Sample preparation

We have performed local analysis by cross-sectional TEM for two BFO films of representative thicknesses (7 and 56 nm) grown by pulsed laser deposition (PLD) under the very same conditions on LAO substrates [23]. Based on the bulk pseudocubic lattice parameters ($a_{LAO} = 0.379$ nm, $a_{BFO} = 0.398$ nm), the lattice mismatch of about 4.5% results in a compressive stress for BFO which is at the origin of the giant tetragonal distortion of the T phase.

Transmission electron microscopy $[100]_{pseudocubic}$-oriented cross-sectional samples were prepared by a classical method combining mechanical polishing and ion milling. Parallel-side slices of roughly 7 μm were obtained by tripod polishing and then argon-ion milled during a couple of hours with a Gatan-PIPS at 2.5 keV and grazing incidence of $\pm 6°$ to avoid irradiation damage; sequential rotation was employed to minimize preferential thinning of the different materials on each side of the interface. Final thinning was obtained with $\pm 4°$ grazing incidence to produce the wide thin areas, uniform in thickness, that are required for STEM-EELS investigations [24]. Plasma-cleaning with a hydrogen/oxygen mixture in a Gatan-Solarus was systematically employed to reduce carbon contamination during STEM-EELS experiments.

B. Transmission electron microscopy

Energy filtered selected area electron diffraction (EFSAED) was realized on a JEOL 2200FS microscope fitted with an in-column Omega energy filter and equipped with DITABIS "imaging-plates" (30 Mpx); this setup allows for a high-detection sensitivity at low doses with a rather high dynamic range and an improved signal-to-noise ratio (SNR) as-compared to the one given by our charge-coupled device (CCD) camera.

High-resolution scanning transmission electron microscopy and EELS experiments were performed on an aberration-corrected FEI Titan 80-300 Cubed microscope equipped with an optimized field emission gun (X-FEG) electron source coupled with a monochromator and fitted with Tridiem Gatan Imaging Filter. High-angle annular dark field images were obtained with a convergence semiangle of 17.3 mrad and an inner collection semiangle greater than 60 mrad. The very high stability of the instrument allowed us to obtain HAADF images of high quality allowing further processing (see below). In order to remove the scanning noise artifact which could hamper the quantitative interpretation of the images, sets of two images with the scanning direction rotated by 90° were acquired and compared. Annular bright field images were recorded at 200 keV under the same illumination conditions but with inner collection semiangle equal to 12 mrad. High-resolution-electron energy loss spectroscopy spectrum-images (typically 256×2048 px^2) were acquired at 80 and 200 keV with monochromator settings providing 0.2 eV energy resolution as measured on the full width at half maximum (FWHM) of the zero-loss peak. Typical values of collection semiangles for EELS experiments were ranging between 20 and 30 mrad. The sample thickness in the studied areas was estimated from the EELS signal: the thickness (t) to inelastic mean-free-path (λ) ratio t/λ was found to range between 0.5 and 0.7, which corresponds to a mean thickness of roughly 40 nm (with λ estimated from the effective atomic numbers).

C. Image and signal analysis

Routines used for geometrical phase shift analysis (GPA) [25] of STEM images and multivariate statistical analysis (MSA) [24,26,27] have been developed under the IDL package. Geometrical phase shift analysis was performed on raw STEM images without any preprocessing or filtering. Dilatation and rotation maps of the lattice planes have been obtained to measure the c/a ratio in BFO and to evidence structural defects.

Multivariate statistical analysis [principal component analysis (PCA)] was employed on ABF micrographs to improve the SNR after standardization of the contrast of the considered elements. The ABF images were considered as an assembly of 2×2 pseudocubic unit cells instead of a single unit cell (as done in Ref. [12]), to avoid the spatial averaging which would hide the possible differences between neighboring unit cells. The first components obtained for each dataset are thus representative of the average contrast of this 2×2 unit-cell

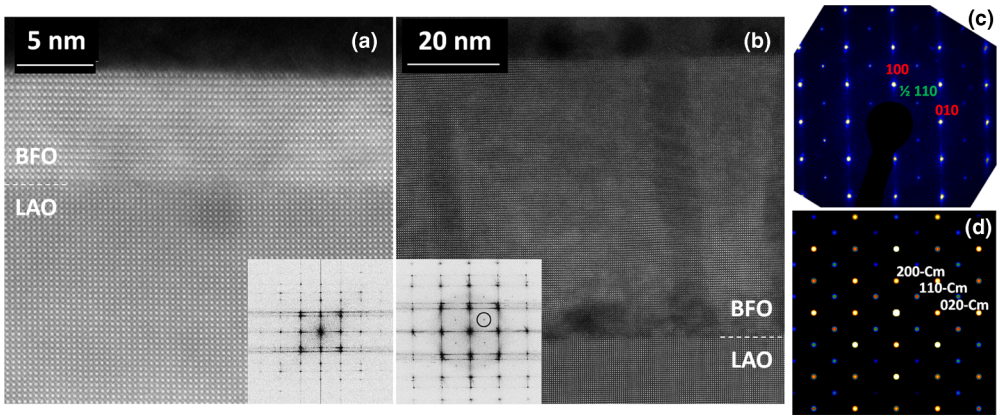

FIG. 1. (Color online) (a) HAADF-STEM image of the 7-nm-thin BFO film on LAO (bottom part of the image). (b) Overview of the 56-nm-thick BFO film showing the Moiré pattern in vertical grain boundaries. Corresponding diffractogram are in insets: circle in (b) points out the ½ $(110)_{pc}$ extraspots. (c) EF-SAED pattern of the 56-nm-thick sample indexed in the pseudocubic notation. (d) Simulated diffraction pattern of the [001]-oriented *Cm* structure of BFO [5] showing the ½ $(110)_{pc}$ extraspots (110-*Cm*).

elements, keeping the variance between neighboring unit cells and allowing one to distinguish the *Cm* and *Cc* phases. In this paper, we restrict our use of the MSA to a statistical noise filtering. Apart from additional insights (not presented here), a detailed analysis of the principal components lead us to keep up to the 10 main components for the image noise filtering.

For fine structure analysis of the O-K and Fe-L_{23} edges, MSA was also applied after background extrapolation with a power law and subtraction to limit the number of components involved in the reconstruction (in a few cases, the background was kept before MSA to improve the power-law extrapolation). The number of components involved for the noise filtering of the signal was determined by a trial-and-error method until the residual between raw data and reconstructed signal does not show any spatial localization. Five to seven components were typically considered for the reconstruction of the dataset (up to 12 when background was not previously subtracted).

III. RESULTS AND DISCUSSION

A. Microstructural analysis of BFO films

Figure 1(a) shows a HR HAADF-STEM image of the 7-nm-thin film. At first glance, this image reveals the high quality of the epitaxial growth of BFO on LAO. One can observe that its diffractogram [inset of Fig. 1(a)] only exhibits the fundamental reflections of a single unit cell of a pseudocubic perovskite (i.e. including only one single formula unit ABO_3). In the thicker film (56-nm-thick), the situation is rather different. Two kinds of areas can be observed: wide T-like areas with grain boundaries perpendicular to the film/substrate interface, appearing as dark bands and exhibiting a Moiré-like pattern [Fig. 1(b)]; slanted R-like grains surrounded by a T-like matrix (see below) already reported in previous studies [2,11,12]. For the thicker film, the corresponding diffractograms [insets of Fig. 1(b)] reveal the presence of extrareflections at $½(110)_{pseudocubic}$ (although not mentioned in the text, these spots are visible in Ref. [2,12]) suggesting a doubling of the unit cell of BFO; it is worth mentioning that such spots are visible even when a few unit cells (down to 6 × 6) are considered to obtain the diffractogram. These extrareflections are also observed on the EF-SAED pattern shown in Fig. 1(c), ruling out the hypothesis of an image-processing artifact and confirming their crystallographic origin. Figure 1(d) shows a dynamic simulation [28] of the diffraction pattern of the *Cm* structure proposed in Ref. [5] and oriented along its [001]-*Cm* direction (Wyckoff positions are taken from this reference while the lattice parameters have been determined in the following); the $½(110)_{pseudocubic}$ (labeled 110-*Cm*) are clearly visible. Figure 2(a) shows an R-like phase grain embedded in a T-like phase matrix; the extrareflections mentioned above are also observed in its diffractogram (not shown). The digital dark field (DDF) obtained by Bragg filtering of the extraspots reveals that these spots arise from the T-like phase. The c/a ratio maps derived from the GPA method [Figs. 2(c) and 2(d)] obtained for both thin and thick films confirm [Figs. 1(a) and 2(a)] the huge c/a expansion close to 1.24 for both thin and thick films in agreement with the literature [7,12]. The map [Fig. 2(c)] confirms the small c/a expansion (less than 1.05) for the R-like phase. The rotation maps of the growing planes $(001)_{pc}$ are shown in Figs. 2(e) and 2(f) for the thick film and the thin film, respectively. The $(001)_{pc}$ planes of the T phase are rotated by less than 0.5° for both films with respect to the (001) planes of the substrate for both samples [Figs. 2(e) and 2(f)]. As already reported [11,12], in the R-like region of the thick film, these planes are rotated by about 3° with respect to the substrate surface. Based on this analysis, the 7-nm-thin film appears to be a single crystal of a T phase of BFO epitaxially strained on the LAO lattice with a "cube-on-cube" geometry. This result is in contrast with the continuous c/a expansion reported in Ref. [21]. The microstructure of the thicker film appears more complex.

Thus, at first glance, our samples appear in perfect agreement with data already published in the literature for the thin samples [7] and thick samples [11,12]. However, we would like to emphasize some new specific features. Figures 3(a) and 3(b), respectively, show a higher magnification of the interface between the LAO substrate and the 56-nm-thick BFO and its diffractogram. As described above, the DDF reconstructed from the extrareflections [green circle in Fig. 3(b)] reveals the location of the sample where this specific pattern is generated

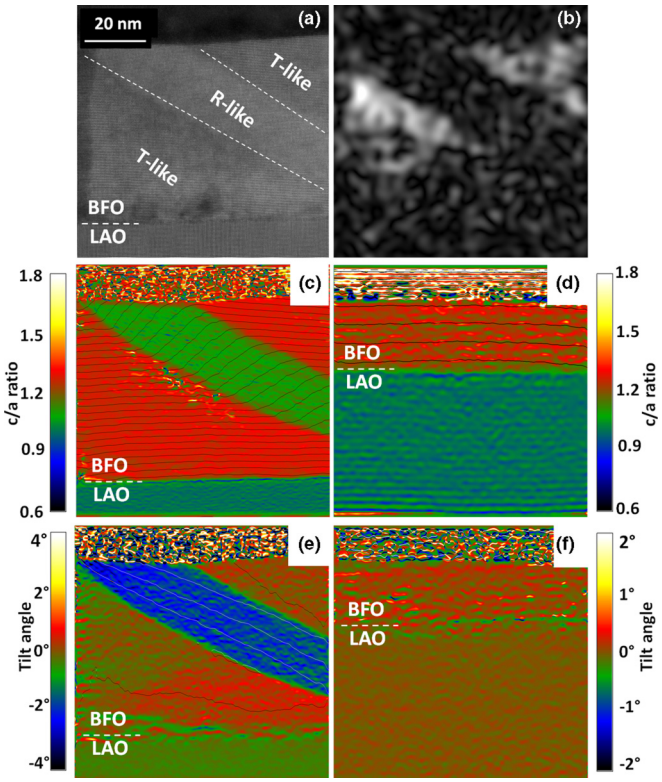

FIG. 2. (Color online) (a) Slanted *R*-like phase grains surrounded by a *T*-like phase matrix in a 56-nm BFO thick film. (b) DDF obtained from the $\frac{1}{2}(110)_{pc}$ extraspot. (c) and (d) c/a ratio maps from, respectively, Figs. 2(a) and 1(a). (e) and (f) Rotation maps of the $(001)_{pc}$ growing planes from, respectively, Figs. 2(a) and 1(a).

[bright area on the right-hand side of Fig. 3(c)]. Again, the GPA performed with the spots squared in red on Fig. 3(b) produces a phase-shift image [Fig. 3(d)] for the growing planes that is consistent with a homogeneous out-of-plane lattice dilatation ($c/a = 1.24$) of the *T*-like phase over the whole film thickness. In addition, we observe a modulation in the rotation map [Fig. 3(e)] obtained from the lattice planes perpendicular to the interface [blue square in Fig. 3(b)]. This map reveals that the location where the tilt of the planes occurs, on the left-hand side of the micrograph, is anticorrelated with the presence of the $\frac{1}{2}(110)_{pseudocubic}$ extraspots present on the right-hand side of the micrograph. The angles measured on this map (5° to 6°) are in agreement with the tilt allowed by the structure shown in Fig. 3(g). This kind of contrast has already been reported in Ref. [12]; however, the modulation was mainly due to the scanning noise. This last hypothesis can be safely ruled out in our experimental setup by rotating the scanning direction by 90° and by comparing STEM images to HR-TEM micrographs in which no scanning noise is expected (not shown). Moreover, this structural modulation is clearly revealed in off-zone-axis EF-SAED [Fig. 3(f)]. The length of this modulation (not perfectly periodic) ranges between 5 and 11 nm as measured on tilt maps and EF-SAED patterns. The Moiré-like pattern [29] observed in Fig. 1(b) is thus interpreted as an interference phenomenon between lattice planes of grains overlapping along the thickness of the TEM sample, the latter being alternatively tilted by about −3° or +3° with respect to the interface normal.

These results unambiguously demonstrate that the extrareflections originate from a *T* phase of different nature to the one observed in the 7-nm-thin film, despite the virtually same lattice parameters (within a few picometers based on our GPA measurements). Among the various phases predicted by first-principles calculations [5], only one space group is consistent with the presence of the $\frac{1}{2}(110)_{pseudocubic}$ extrareflections: the *Cm* space group (as suggested in Ref. [11]) observed along the [001] azimuth [Fig. 3(g)] with $a = 0.9475$ nm, $b = 0.758$ nm, $c = 0.379$ nm as measured from the GPA analysis. None of the other crystallographic directions of any of the possible structures in the references above [5,13] lead to this specific diffraction pattern.

Based on a large sampling of images from the films, it is possible to conclude that thick films mainly crystallize in a *T*-like phase with some inclusions of *R*-like phase. This structure is likely due to a stress relaxation process occurring at a critical thickness of a few tens of nanometers. Thus, we propose that the *T* phase present in thick films crystallizes in the *Cm* space group. This phase is observed along either the [001] direction (with extrareflections, *c*-oriented grains) or along the [010] direction (showing a classical perovskite pattern, *b*-oriented grains).

B. Atomic structure of the *T*-like phase in thick BFO films

The previous finding is supported by the ABF-STEM images [raw data is presented in Fig. 4(a)]. The ABF technique enhances the contrast from atomic columns of light elements; it has been successfully employed to detect the position of light elements in materials and especially the geometry of oxygen octahedra at interfaces in oxides [30]. In our case, the position of the oxygen atoms in the BFO unit cell, with respect to the heavy surrounding elements Fe and Bi, is probed to determine the Fe-O geometry. Figure 4(b) shows an ABF image processed by MSA [26] to improve the signal-to-noise ratio (SNR). The O atoms located in the Fe-O_2 plane and close to the Bi are barely visible: the most distant O from Bi appear as a tail on the side of the Bi [blue arrow on Fig. 4(c)], while the closest ones are not resolved; the apical O atoms are easier to detect as they are rather distant from the heavy Fe and Bi ones [black arrows on Fig. 4(c)]. Thus, their shift with respect to the regular octahedral position is evidenced. The shift upward from the central position of the Fe atoms is also obvious. As presented on Fig. 4(d), the atom positions in the *Cm* structure [5] match relatively well the ABF contrast, confirming the presence of FeO_5 pyramids pointing toward the substrate instead of FeO_6 octahedra. Viewed along the [001]-*Cm* direction, their projection are alternatively tilted on the right-hand side and on the left-hand side in neighboring ABO_3 cells (M_3^+ in phase mode in one direction) contrary to the *Cc* structure for which the neighboring the ABO_3 cells appear identical (due to the projection effect of the R_4^+ out-of-phase symmetry in two directions). The relative positions of atoms can be evaluated from Fig. 3(c): the out-of-plane shift of the Fe atom (with respect to the center of the Bi cage) was found to be roughly 33 ± 6 pm, whereas the in-plane shift was zero within the accuracy of our measurements. For the apical O, the

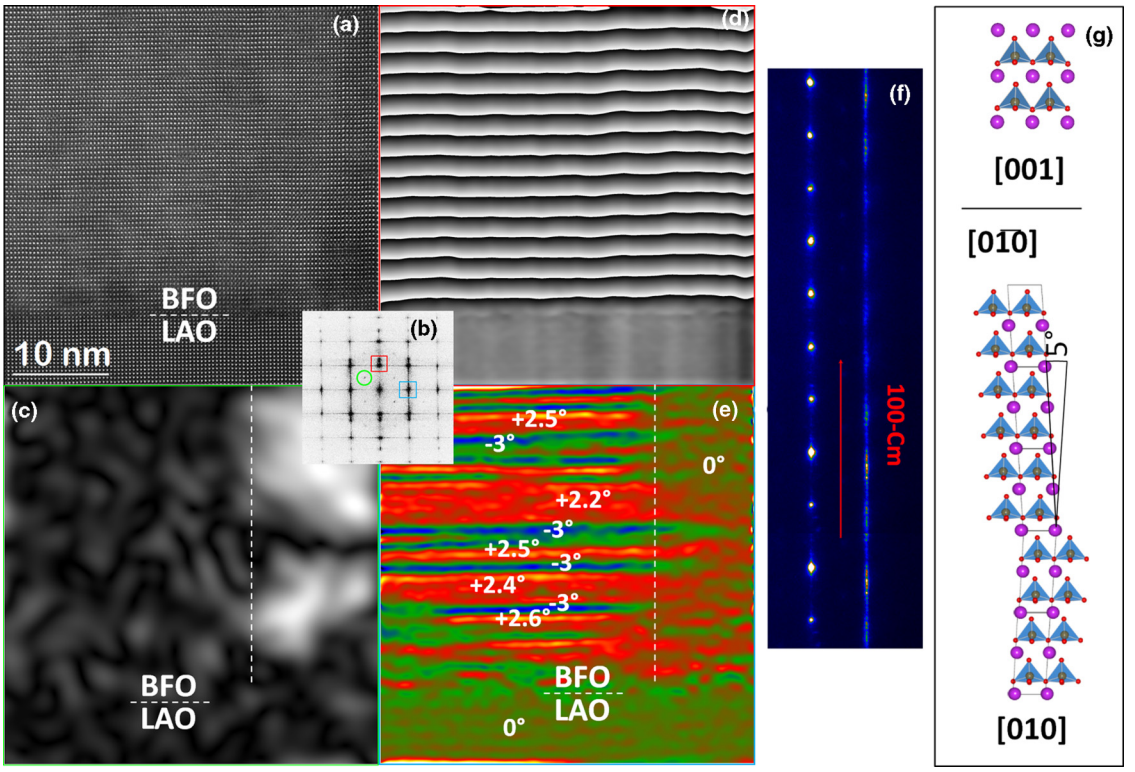

FIG. 3. (Color online) (a) Magnification of the 56-nm BFO/LAO interface. (b) Corresponding fast Fourier transform.(c) DDF obtained with the spot circled in green in (b) showing the presence of a [001]-oriented grain (white area on the right-hand side). (d) Phase-shift image of the (100)-*Cm* growing planes evidencing the homogeneity of the $c/a = 1.24$ strain across the grain boundary [dotted line in (c)]. (e) Tilt map of the (001)-*Cm* growing planes in the [010]-oriented grain. (f) 8°-off [010] EF-SAED pattern showing the intensity modulation along the [100]-*Cm* growing direction. (g) The *Cm* structure of BFO in the [001] projection (top) and in the [010] and [0-10] projections with a microtwin (bottom).

out-of-plane shift with respect to the Bi plane was close to 73 ± 8 pm, and the in-plane shift (with respect to the Fe plane, i.e. the middle of the Bi-Bi distance) was ranging between 10 ± 8 pm for the less shifted atoms and 20 ± 8 pm for the most shifted. These values are in agreement with the *Cm* structure in which the Fe out-of-plane shift is 29 pm and the apical O shifts with respect to the middle of the Bi-Bi are 81 and 8 pm, respectively, out-of-plane and in-plane.

This *Cm* structure associated with the rather complex microstructure depicted above can potentially explain the deviation from the expected multiferroic properties of such thick films [10]. Indeed, instead of being single crystalline,

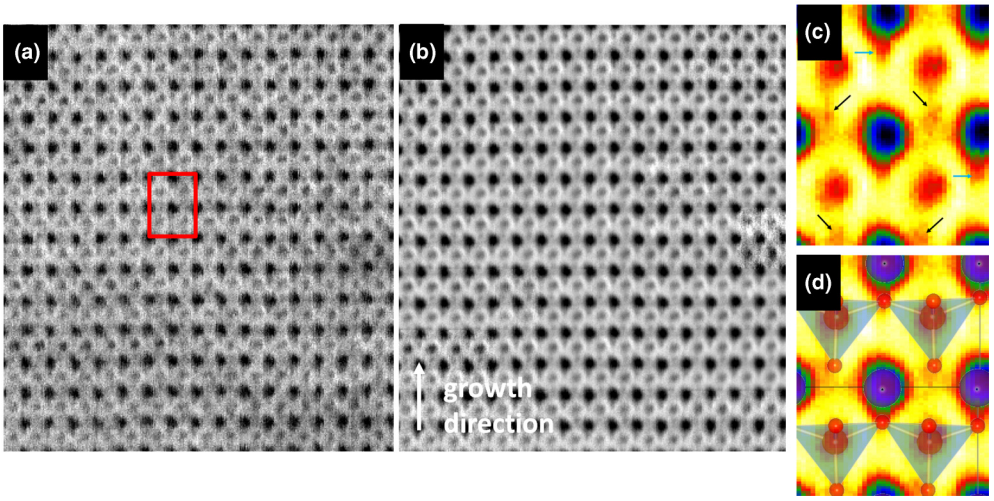

FIG. 4. (Color online) (a) Raw ABF-STEM image showing the shift of the apical oxygen and of the iron. The elemental unit cell considered for MSA processing is depicted in red. (b) ABF-STEM image of the 56-nm-thick BFO film. (c) First component of the MSA; arrows point the position of oxygen atoms. (d) The proposed *Cm* structure superimposed on (c).

the T-like volume of the sample is composed of two families of grains, crystallized in the *Cm* space group and rotated by 90° (as a consequence of the symmetry of the substrate). In each grain, the BFO unit cell experiences several 180° in-plane rotations leading to a stacking of microtwins over the thickness of the film. To our knowledge, this specific microstructure has not yet been revealed by x-ray diffraction experiments, most probably because of the nanometric size (2 to 5 nm) of these microtwins. Together with the presence of R-like inclusions, this microstructure thus renders the interpretation of magnetic and polarization measurements more convoluted than expected from a simplistic view of the structure. Based on a single crystal analysis, for the *Cc* phase, the in-plane spontaneous polarization is expected to point toward the $[110]_{\text{pseudocubic}}$ direction, whereas it would point toward the [010] direction for the *Cm* phase. The effect of the microtwins on the spontaneous polarization is delicate to handle, but it would probably strongly modify the situation described above.

C. EELS analysis

In order to gain further insight on the T-phase structure, monochromated EELS line scans were acquired with an energy resolution of 0.2 eV [31] for O-K, Fe-L_{23}, and La-M_{45} edges. After SNR improvement by MSA [27], elemental profiles for La and Fe were obtained and revealed the chemical sharpness of the interface. For the thick sample, no changes of the fine structures of the O-K or the Fe-L_{23} edges were observed in the *Cm* phase over the whole thickness of the film, indicating that, if distortions of the Fe-O_5 pyramid occur, they are sufficiently weak not to perturb the EELS signal. This suggests that the electronic structure of the material is preserved over the whole thickness (i.e. the Fe-O and O-Bi bonding remain unchanged, suggesting that the bonding environment is maintained across the film thickness).

The situation is drastically different in the case of the thinnest film. Despite the similarly sharp interface as in the case of the thickest film, significant differences are present and worth rediscussing.

The O-K and the Fe-L_{23} edge fine structures [Figs. 5(a) and 5(b), respectively] evolve from the interface to the surface of the film. Based on previous *ab initio* calculations [12,32–35], it is possible to identify the various features in the spectra. Peak A2 is related to transition to the hybridized O 2p-Bi 5d orbitals instead of the commonly observed crystal-field splitting due to the octahedral geometry of oxygen around the transition metal (transition to the O 2p-Fe 3d hybridized orbitals); the crystal-field splitting in bulk BFO has hardly been resolved even with 0.2 eV energy resolution [32,35] and is contained in the A1 peak. In a similar way, the crystal field splitting is contained in the Fe-L_3 and Fe-L_2 peaks stemming from Fe2p3/2 and Fe2p1/2 to O2p-Fe3d hybridized orbitals. Close to the interface, peak A2 in the O-K edge is strongly enhanced, while a shoulder appears on the low-energy side of the Fe-L_3 edge in the upper part of the film (a more pronounced shoulder was observed in the *Cm* phase of the thickest film). Multilinear fit of the dataset with specific fingerprints was employed in order to map the fine structures. For the O-K edge, three components were considered: one representative of the substrate, a second one associated with the A2 peak (i.e. in which the A2/A1 ratio is close to 1), and a third one with a weaker A2/A1 ratio. Two components were considered for the Fe-L_{23} edge: one with the shoulder on the low-energy side of the L_3 peak, another one in which this shoulder is not observed. The map [Fig. 5(c)] reveal an apparent interface width of roughly 1.5 nm (measured on the O_{LAO} profile) to be compared to the 0.4 nm of the perovskite unit cell. This apparent width is compatible with an atomically sharp interface if one considers the broadening of the highly convergent probe ($\alpha/2 = 18$ mrad) over the thin foil thickness t ($t = 40$ nm). It is worth noting that this width is about two times narrower than the one reported in Ref. [22] and estimated from the Fe-L_{23} and La-M_{45} integrated intensity; using the same procedure (not shown), we have measured an interface width of 1.5 nm, confirming that cationic interdiffusion has not exceed three pseudocubic unit cells. This narrower interface width compare to the one reported in Refs. [21,22] could results from differences in the growing conditions (our samples being grown at a lower temperature of 580 °C). The map in Fig. 5(c) also reveals a smooth evolution of the O-K edge features from the interface to the surface. While the increase of the A2 structure would indicate a change in the Bi-O bonding, the weakening of the shoulder on the Fe-L_3 edge close to the interface suggests a slight modification of the Fe-O configuration: a modification of the crystal field resulting in a distortion of FeO_5 pyramids described above by the underlying symmetry imposed by the LAO substrate appears as the most likely explanation.

This shows that the picture of a phase stabilized near the interface through simple biaxial mechanical strain is not sufficient to explain the behavior of BFO films. Indeed, elemental profiles do not show any stoichiometric fluctuations. The AlO_6 octahedra geometry in the LAO could constrain the first layers of BFO to adopt a specific organization by limiting the pyramidal tilts as already proposed for similar systems [15–17]. The influence of such antiferrodistortive coupling across the interface was demonstrated in Ref. [16], triggering a suppression of the octahedral tilting over two nanometers away from the film/buffer interface. Our results suggest that, below a critical thickness (about 4 nm), BFO films grown on LAO can be purely tetragonal ($P4mm$) and single crystalline; such a film would exhibit the highest out-of-plane spontaneous polarization.

An interpretation of our results can then be based on the framework proposed by Christen *et al.* [19] where a sequence of phase transitions from an R phase to a T phase is described as a function of a purely biaxial stress imposed on BFO and by considering the additional stress induced by atomic structure of the substrate. The thinnest film, highly stressed by the substrate, owing to the lattice-parameter misfit and octahedral geometry, is thus composed of a T-like phase, which does not exhibit microtwins but experiences different levels of strain: the lower part being close to a $P4mm$ purely tetragonal phase and the upper part of the film (slightly relaxed) being close to a *Cm* phase. In Ref. [19], the $P4mm$ phase was stabilized with a 10% purely biaxial stress to be compared to the 4.5% imposed by LAO, but the underlying atomic structure was not considered. The thickest film is a mixture of two phases coming from different level relaxation of a fully strained and purely tetragonal $P4mm$ phase. A microtwinned T-like phase monoclinically distorted (coming from a slight relaxation of

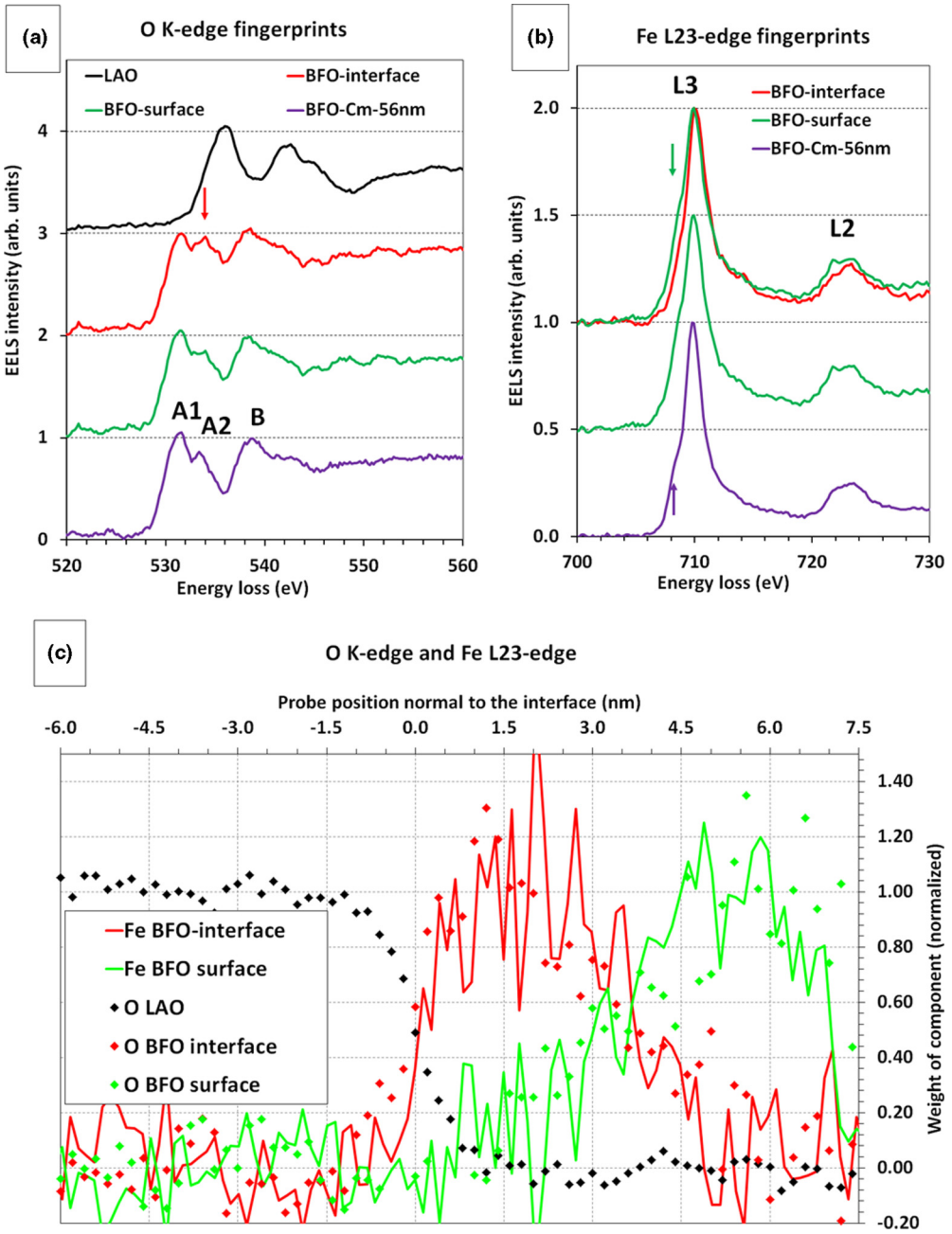

FIG. 5. (Color online) (a) O-K edge fingerprints recorded on the 7-nm-thick film showing the enhancement of the A2 structure in the vicinity of the interface with the substrate. (b) Fe-L_{23} edge fingerprints acquired in the same area showing a shoulder (arrows) on the low-energy side of the L_3 peak. O-K and Fe-L_{23} Fingerprints of the Cm phase, recorded on the 56-nm sample, are displayed in purple for comparison. (c) Normalized weights of the fingerprints obtained by a multilinear fit of the dataset.

the $P4mm$ phase leading to the Cm geometry) coexists with an R-like phase (strong relaxation of the $P4mm$ leading to a phase close to the $R3c$ bulk phase).

IV. CONCLUSION

In conclusion, although the influence of film thickness on the BFO crystal structure was already mentioned in the literature [7,8,13,21,36,37], we provide new insights on BFO crystal structure. Namely, we have shown that the highly strained BFO films exhibit a crystallographic structure strongly dependent on the deposited thickness. The c/a ratio is not a relevant parameter to classify BFO thin films [38]: despite an identical c/a distortion ($c/a = 1.24$), slight variations have been evidenced between the 7-nm-thin and the 56-nm-thick film. A Cm phase has been demonstrated by a combination of EF-SAED and ABF-STEM approaches, in agreement with first-principles calculations [5,6]. Structural and microstructural departures between the thin and thick films have been evidenced by GPA analysis of STEM images, and slight modifications of the atomic structure of the T-like phase was confirmed by EELS. Microtwinning of the Cm

phase was revealed in the thicker and most relaxed film. The virtually single crystalline thin film is in fact composed of a gradually strained T-like phase, the closest area to the film/substrate interface, about 4 nm thick, pointing toward a $P4mm$ phase. The combination of experimental techniques and the thorough quantitative analysis of the data employed in this paper thus provide a picture on the atomic structures and microstructures of highly strained BFO films; this sheds a light on the interpretation of polarization measurement of such BFO films. The understanding of multiferroic properties of such BFO films thus appears more complex than the defect-free scheme commonly adopted. Our findings are relevant for devices based on thin T-like BFO films, such as ferroelectric tunnel junctions [39,40] and field-effect transistors [41], and more generally for the elucidation of delicate structural issues, ubiquitous in ultrathin oxide films and interfaces [42,43].

ACKNOWLEDGMENTS

Part of this work was carried out at the Canadian Centre for Electron Microscopy, a facility supported by McMaster University and NSERC. GAB is grateful to NSERC for a Discovery grant supporting this work. F.P. gratefully acknowledges Région Poitou-Charente for an invited scientist grant. Some of the authors acknowledge financial support from the European Research Council (ERC Advanced Grant FEMMES, No. 267579) and the French Agence Nationale de la Recherche (ANR) through projects NOMILOPS and MULTIDOLLS.

[1] J. B. Neaton, C. Ederer, U. V. Waghmare, N. A. Spaldin, and K. M. Rabe, Phys Rev. B **71**, 014113 (2005).
[2] R. J. Zeches, M. D. Rossell, J. X. Zhang, A. J. Hatt, Q. He, C.-H. Yang, A. Kumar, C. H. Wang, A. Melville, C. Adamo, G. Sheng, Y.-H. Chu, J. F. Ihlefeld, R. Erni, C. Ederer, V. Gopalan, L. Q. Chen, D. G. Schlom, N. A. Spaldin, L. W. Martin, and R. Ramesh, Science **326**, 977 (2009).
[3] I. Sosnowska, T. Peterlin-Neumaier, and E. Steichele, J. Phys. C: Solid State Phys. **15**, 4835 (1982).
[4] C. Ederer and N. A. Spaldin, Phys. Rev. B **71**, 060401 (2005).
[5] O. Dieguez, O. E. Gonzales-Vasquez, J. C. Wojdel, and J. Iniguez, Phys. Rev. B. **83**, 094105 (2011).
[6] B. Dupé, I. C. Infante, G. Geneste, P.-E. Janolin, M. Bibes, A. Barthélémy, S. Lisenkov, L. Bellaiche, S. Ravy, and B. Dkhil, Phys. Rev. B **81**, 144128 (2010).
[7] H. Béa, B. Dupé, S. Fusil, R. Mattana, E. Jacquet, B. Warot-Fontrose, F. Wilhelm, A. Rogalev, S. Petit, V. Cros, A. Anane, F. Petroff, K. Bouzehouane, G. Geneste, B. Dkhil, S. Lisenkov, I. Ponomareva, L. Bellaiche, M. Bibes, and A. Barthélémy, Phys. Rev. Lett. **102**, 217603 (2009).
[8] Z. Chen, Z. Luo, Y. Qi, P. Yang, S. Wu, C. Huang, T. Wu, J. Wang, C. Gao, T. Sritharan, and L. Chen, Appl. Phys. Lett. **97**, 242903 (2010).
[9] R. Jarrier, X. Marty, J. Herrero-Albillos, P. Ferrer, R. Haumont, P. Gemeiner, G. Geneste, P. Berthet, T. Schülli, P. Cevc, R. Blinc, S. S. Wong, T. J. Park, M. Alexe, M. A. Carpenter, J. F. Scott, G. Catalan, and B. Dkhil, Phys. Rev. B **85**, 184104 (2012).
[10] J. X. Zhang, Q. He, M. Trassin, W. Luo, D. Yi, M. D. Rossel, P. Yu, L. You, C. H. Wang, C. Y. Kuo J. T. Heron, Z. Hu, R. J. Zeches, H. J. Lin, A. Tanaka, C. T. Chen, L. H. Tjeng, Y. H. Chu, and R. Ramesh, Phys. Rev. Lett. **107**, 147602 (2011).
[11] I. C. Infante, J. Jurasek, S. Fusil, B. Dupé, P. Gemeiner, O. Diéguez, F. Pailloux, S. Jouen, E. Jacquet, G. Geneste, J. Pacaud, J. Iñiguez, L. Bellaiche, A. Barthélémy, B. Dkhil, and M. Bibes, Phys. Rev. Lett. **107**, 237601 (2011).
[12] M. D. Rossel, R. Erni, M. P. Prange, J. C. Idrobo, W. Luo, R. J. Zeches, S. T. Pantelides, and R. Ramesh, Phys. Rev. Lett. **108**, 047601 (2012).
[13] C.-J. Cheng, C. Lu, Z. Chen, L. You, L. Chen, J. Wang, and T. Wu, Appl. Phys. Lett. **98**, 242502 (2011).
[14] Q. He, Y. H. Chu, J. T. Heron, S. Y. Yang, W. I. Liang, C. Y. Kuo, H. J. Lin, P. Yu, C. W. Liang, R. J. Zeches, W. C. Kuo, J. Y. Juang, C. T. Chen, E. Arenholz, A. Scholl, and R. Ramesh, Nat. Commun. **2**, 225 (2011).
[15] Y. Yang, C. Schlepütz, C. Adamo, D. G. Schlom, and R. Clarke, APL Mater. **1**, 052102 (2013).
[16] A. Y. Borisevitch, H. J. Chang, M. Huijben, M. P. Oxley, S. Okamoto, M. K. Niranjan, J. D. Burton, E. Y. Tsymbal, Y. H. Chu, P. Yu, R. Ramesh, S. V. Kalinin, and S. Pennycook, Phys. Rev. Lett. **105**, 087204 (2010).
[17] J. M. Rondinelli and N. A. Spaldin, Phys. Rev. B **82**, 113402 (2010).
[18] C. Daumont, W. Ren, I. C. Infante, S. Lisenkov, J. Allibe, C. Carrétéro, S. Fusil, E. Jacquet, T. Bouvet, F. Bouamrane, S. Prosandeev, G. Geneste, B. Dkhil, L. Bellaiche, A. Barthélémy, and M. Bibes, J. Pys.: Condens. Matter. **24**, 162202 (2012).
[19] H. M. Christen, J. H. Nam, H. S. Kim, A. J. Hatt, and N. Spaldin, Phys. Rev. B **83**, 144107 (2011).
[20] A. Hatt, N. A. Spaldin, and C. Ederer, Phys. Rev. B **81**, 054109 (2010).
[21] R. Huang, H.-C. Ding, W. I. Liang, Y.-C. Gao, X. D. Tang, Q. He, C. G. Duan, Z. Zhu, J. Chu, C. A. J. Fisher, T. Hirayama, Y. Ikuhara, and Y. H. Chu, Adv. Funct. Mater. **24**, 793 (2014).
[22] P. S. Sankara Rama Krishnan, A. N. Morozovska, E. A. Eliseev, Q. M. Ramasse, D. Kepaptsoglou, W. I. LIang, Y. H. Chu, P. Munroe, and V. Nagarajan, J. Appl. Phys. **115**, 054103 (2014).
[23] H. Béa, M. Bibes, A. Barthélémy, K. Bouzehouane, E. Jacquet, A. Khodan, J. P. Contour, S. Fusil, F. Wyczisk, A. Forget, D. Lebeugle, D. Colson, and M. Viret, Appl. Phys. Lett. **87**,072508 (2005).
[24] F. Pailloux, D. Imhoff, T. Sikora, A. Barthélémy, J. L. Maurice, J. P. Contour, C. Colliex, and A. Fert, Phys. Rev. B **66**, 014417 (2002).
[25] M. J. Hÿtch, E. Snoeck, and R. Kilaas, Ultramicroscopy **74**, 131 (1998).
[26] J. L. Maurice, F. Pailloux, D. imhoff, N. Bonnet, L. Sammet, A. Barthélémy, J. P. Contour, C. Colliex, and A. Fert, Eur. Phys. J. Appl. Phys. **24**, 215 (2003).
[27] N. Bonnet, Ultramicrscopy **77**, 97 (1999).

[28] P. A. Stadelmann, Ultramicroscopy **21**, 131 (1987), http://cimewww.epfl.ch/people/Stadelmann/jemsWebSite/jems.html.
[29] D. W. Pashley, Phil. Mag. **4**, 324 (1959).
[30] S. Zheng, C. A. J. Fisher, T. Kato, Y. Nagao, H. Ohta, and, Y. Ikuhara, Appl. Phys. Lett. **101**, 191602 (2012).
[31] G. A. Botton, S. Lazar, M.-Y. Wu, F. D. Tichelaar and H. W. Zandbergen, Microscopy and Microanalysis **9**, 112 (2003).
[32] T. J. Park, S. Sambasivan, D. A. Fisher, W. S. Yoon, J. A. Misewich, and S. S. Wong, J. Phys. Chem C **112**, 10359 (2008).
[33] R. Saeterli, S. M. Selbach, P. Ravindran, T. Grande, and R. Holmestad, Phys. Rev. B **82**, 064102 (2010).
[34] A. Y. Borisevich, E. A. Eliseev, A. N. Morozovska, C. J. Cheng, J. Y. Lin, Y. H. Chu, D. Kan, I. Takeuchi, V. Nagarajan, and S. V. Kalinin, Nature Commun. **3**, 775 (2012).
[35] T. Higuchi, Y.-S. Liu, P. Yao, P.-A. Glans, J. Guo, C. Chang, Z. Wu, W. Sakamoto, N. Itoh, T. Shimura, T. Yogo, and T. Hattori, Phys. Rev. B **78**, 085106 (2008).
[36] C. J. C. Bennett, H. S. Kim, M. Varela, M. D. Biegalski, D. H. Kim, D. P. Norton, H. M. Meyer, III, and H. M. Christen, J. Mater. Res. **26**, 1326 (2011).
[37] C. Beekman, W. Siemons, T. Z. Ward, M. Chi, J. Howe, M. D. Biegalski, N. Balke, P. Mksymovych, A. K. Farrar, J. B. Romero, P. Gao, W. Q. Pan, D. A. Tenne, and H. M. Christen, Adv. Mater. **25**, 5561 (2013).
[38] J. E. Rault, W. Ren, S. Prosendeev, S. Lisenkov, D. Sando, S. Fusil, M. Bibes, A. Barthélémy, L. Bellaiche, and N. Barrett, Phys. Rev. Lett. **109**, 267601 (2012).
[39] H. Yamada, V. Garcia, S. Fusil, S. Boyn, M. Marinova, A. Gloter, S. Xavier, J. Grollier, E. Jacquet, C. Carrétéro, C. Deranlot, M. Bibes, and A. Barthélémy, ACS Nano **7**, 5385 (2013).
[40] E. Y. Tsymbal, A. Gruverman, V. Garcia, M. Bibes, and A. Barthélémy, MRS Bull. **37**, 138 (2012).
[41] H. Yamada, M. Marinova, P. Altuntas, A. Crassous, L. Bégon-Lours, S. Fusil, E. Jacquet, V. Garcia, K. Bouzehouane, A. Gloter, J. E. Villegas, A. Barthélémy, and M. Bibes, Scientific Reports **3**, 2834 (2013).
[42] M. Bibes, J. E. Villegas, and A. Barthélémy, Adv. Phys. **60**, 5 (2011).
[43] P. Zubko, S. Gariglio, M. Gabay, P. Ghosez, and J.-M. Triscone, Annu. Rev. Condens. Matter Phys. **2**, 141 (2011).